ACS OMEGA

http://pubs.acs.org/journal/acsodf

Article

Mixed Cu–Fe Sulfides Derived from Polydopamine-Coated Prussian Blue Analogue as a Lithium-Ion Battery Electrode

Behnoosh Bornamehr, Volker Presser,* and Samantha Husmann*

Cite This: *ACS Omega* 2022, 7, 38674–38685

Read Online

ACCESS | Metrics & More | Article Recommendations | Supporting Information

ABSTRACT: Batteries employing transition-metal sulfides enable high-charge storage capacities, but polysulfide shuttling and volume expansion cause structural disintegration and early capacity fading. The design of heterostructures combining metal sulfides and carbon with an optimized morphology can effectively address these issues. Our work introduces dopamine-coated copper Prussian blue (CuPB) analogue as a template to prepare nanostructured mixed copper–iron sulfide electrodes. The material was prepared by coprecipitation of CuPB with in situ dopamine polymerization, followed by thermal sulfidation. Dopamine controls the particle size and favors K-rich CuPB due to its polymerization mechanism. While the presence of the coating prevents particle agglomeration during thermal sulfidation, its thickness demonstrates a key effect on the electrochemical performance of the derived sulfides. After a two-step activation process during cycling, the C-coated $KCuFeS_2$ electrodes showed capacities up to 800 mAh/g at 10 mA/g with nearly 100% capacity recovery after rate handling and a capacity of 380 mAh/g at 250 mA/g after 500 cycles.

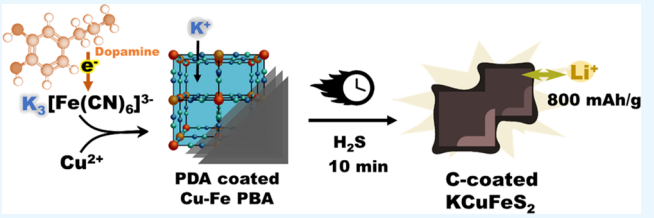

1. INTRODUCTION

Lithium-ion batteries (LIBs) are essential technologies to carry present-day electrochemical charge storage in stationary and portable applications.[1,2] Common cathode materials employ metal oxides composed of cobalt, nickel, and manganese with a layered structure that allows the facile, reversible, and electrochemically triggered insertion of Li^+ ions between the layers with typical capacities of about 200 mAh/g.[3−5] Elements such as cobalt and nickel are less common, cost drivers, and subject to geopolitical considerations and can be replaced by more common and widely available elements, such as copper and iron. Still, the low capacities of metal oxides commonly used in commercial batteries limit the performance, and other compounds are relevant to the investigation for achieving a higher energy density.[6]

Metal sulfides are actively explored to replace transition-metal oxides in new battery technologies.[7,8] These compounds can undergo conversion reactions in addition to insertion and enable redox processes that transfer more electrons and therefore provide higher charge storage capacity.[9] They are also more thermally stable and electronically conductive than their oxide counterparts.[10,11] Copper iron sulfide is particularly attractive as it is nontoxic, cheap, and provides high natural abundance of its elements.[12] The material potential for use in energy storage has been demonstrated in LIB applications. For example, $CuFeS_2$ nanorods have shown high capacities of 633 mAh/g at 0.2 C when tested between 0.01 and 3.0 V vs Li/Li^+ as LIB electrodes.[13]

Standard synthesis methods for these nanosulfides are energy-intensive, lack scalability, or are based on inorganic solvents. Therefore, greener methods to produce metal sulfides can increase the sustainability of electrode production. However, a new synthesis method must be employed while addressing the limitation of the metal sulfides.[8,14] The limiting factors causing performance degradation for metal sulfides are the relatively low electrical conductivity, significant volume expansion, and polysulfide shuttling during electrochemical cycling.[15,16] To mitigate these drawbacks of metal sulfides, different strategies can be pursued. Adding carbon to the material can enhance the conductivity, while homogeneity and interaction in the nanoscale between the components significantly improve the performance.[17−19] Nanodesigned structures can accommodate or buffer the volumetric expansion. Different morphologies have been used, such as hollow, hierarchical, and core–shell structures, or simply reducing the particle size as a strategy.[20] These approaches reduce ion diffusion path and volume expansion resulting from lithiation while trapping polysulfides.[21] There are many methods to produce metal sulfides, but a simple means to incorporate morphology design is by deriving the metal sulfide from a template material.

Prussian blue (PB) is a porous and tunable material that consists of iron centers coordinated by cyanide ligands $(Fe_4[Fe(CN)_6]_3$ or $AFe[Fe(CN)_6]$, where A is an alkali

Received: July 5, 2022
Accepted: September 30, 2022
Published: October 17, 2022

metal).[12] PB synthesis is particularly facile when using a coprecipitation method in water, making it ideal for upscaling. By switching the metallic precursors, Prussian blue analogues (PBAs) can be synthesized, replacing the iron species in the lattice with other transition metals.[22] PB and PBAs can then be used as templates for various derived compounds such as oxides, phosphides, nitrides, alloys, carbides, and chalcogenides, including metal sulfides.[23−26]

In addition, PBAs are also very flexible in morphology design.[27] Different morphologies can be obtained by changing the PB synthesis parameters, such as hollow- or nanostructures and core−shell and hierarchical structures, which can help reduce the effects of volume expansion during cycling.[28] Often, the PBAs are combined with carbon species either by growing PBAs on the surface of conductive carbon substrates or coating PBAs with carbon or carbon precursors. For example, polydopamine (PDA) has been recently established as a coating agent, as it is easy to polymerize in aqueous media and form a coating layer on different substrates.[29,30] Besides aiding in the conductivity and electrochemical stability of PB(A)s, carbon can control the size and morphology of the particles.[31,32] These morphological attributes are then kept after the derivatization procedure. They are of critical importance in the case of metal sulfides for energy storage since they can mitigate volume expansion, increase conductivity, and shorten diffusion paths.[33]

This work reports the successful derivatization of mixed iron−copper sulfide from copper hexacyanoferrate (analogous to PB) while describing the effect of PDA addition and its thickness on the morphology and electrochemical performance. In contrast to previous reports, we show that the PDA coating can be done at acidic pH, and the presence of PDA favors the stabilization of alkali metal ions in the structure. Through self-sacrificial thermal sulfidation, the material is converted into carbon-coated copper−iron sulfides. This enables a one-step water-based template synthesis, coating, and morphology design. Furthermore, complete conversion is achieved within 10 min under a mild temperature of 300 °C, which is, to the best of the authors' knowledge, the fastest for mixed-metal sulfide derivatization while still using a temperature lower than 400 °C. The thickness of the PDA coating plays a crucial role in stabilizing particle growth and morphology, which further determines the derivative performance as a Li-ion battery electrode.

2. EXPERIMENTAL SECTION

2.1. Synthesis of Cu-PBA. Dopamine hydrochloride (type: quality level 200), potassium ferricyanide ($K_3[Fe(CN)_6]$, ≥99.0%), and copper chloride ($CuCl_2$, ≥99.95%) were purchased from Sigma-Aldrich. All aqueous solutions were prepared with ultrapure water (ρ > 18 MΩ·cm), and a pH of 2 was adjusted with concentrated HCl (37%, Sigma). Bare copper hexacyanoferrate (denoted CuPB) was prepared by dropwise addition at a 40 mL/h rate of 100 mL aqueous solution of copper chloride (12.5 mmol/L) to 100 mL aqueous solution of potassium ferricyanide (25 mmol/L) under magnetic stirring. For the PDA-coated samples, 76 mg or 1 g of dopamine hydrochloride was first added to the $K_3[Fe(CN)_6]$ solution under stirring before the addition of $CuCl_2$ solution, yielding samples CuPB-PDA1 and CuPB-PDA2, respectively (Table 1). After the complete addition of $CuCl_2$, the mixture was stirred for 1 h more to ensure homogeneity and set to rest overnight for 18 h. The powder was then collected via centrifugation, washed with distilled water to pH 5, washed twice with acetone, and dried in an oven at 80 °C for 18 h.

Table 1. Synthesis Conditions to Prepare the Copper Hexacyanoferrate Template

	sample		
	CuPB	CuPB-PDA1	CuPB-PDA2
$K_3[Fe(CN)_6]$	100 mL,25 mM, pH 2	100 mL,25 mM, pH 2	100 mL,50 mM, pH 2
$CuCl_2$	100 mL, 12.5 mM,pH 2	100 mL, 12.5 mM,pH 2	100 mL,25 mM, pH 2
dopamine		76 mg(0.5 mmol)	1 g(6.5 mmol)
DAH/Fe (molar ratio)	0	0.1	2.6

2.2. Sulfidation of Cu-PBA. The conversion of CuPB into sulfide was done in a Carbolite Gero H_2S tubular furnace. The CuPB powder was placed in the center of the quartz tube and purged with 100 sccm argon (99.999%) for 2 h. The furnace was heated to 300 °C at a heating rate of 5°/min and an Ar flow of 100 sccm. The temperature was then maintained for 10 min under a flow of 50 sccm of H_2S gas as reactant gas and 100 sccm Ar as protective gas. The product was collected after cooling the furnace to room temperature under 50 sccm of Ar gas flow. The sulfidized samples were denoted with an S to the name, for example, CuPB-S for the sulfidation product from CuPB. The yield after the sulfidation was the highest for the PDA-free sample (80%), and with the PDA increase, the yield decreased due to carbonization of the polymer, with the lowest percentage of 71% for the CuPB-PDA2 sample.

2.3. Material Characterization. Structural morphology was characterized by scanning electron microscopy (SEM) and elemental analysis via energy-dispersive X-ray (EDX) spectroscopy using a ZEISS GEMINI 500 microscope coupled with an X-max detector from Oxford Instruments, employing an acceleration voltage of 1 kV for imaging and 15 kV for spectroscopy. The samples were mounted on an aluminum stub fixed with carbon tape without additional conductive sputter coating. For elemental analysis, at least 20 points were chosen randomly, and the average amount of detected elements was calculated. The average particle size was calculated by measuring 100 particles under focus in the SEM images with the software ImageJ.

A 2100F system (JEOL) at 200 kV was used for transmission electron microscopy (TEM). The powder was dispersed in ethanol via an ultrasonic bath to prepare the samples and then dried on the copper grid coated with lacey carbon drop by drop.

For phase analysis, powder X-ray diffraction (XRD) was performed using a D8 Discover diffractometer (BRUKER AXS) with a copper source (Cu Kα, 40 kV, 40 mA), a Göbel mirror, and a 1 mm point focus. A two-dimensional VANTEC detector was used to cover an angular range of 20° 2θ for 1000 s and repeated three times to record an angular range of 10−80° 2θ. All scans went through background subtraction and were normalized to (0,100). Rietveld refinement was done by HKL fits of the corresponding phases using the software TOPAS 6 from Bruker AXS.

Raman spectroscopy was conducted with a Renishaw inVia Raman microscope employing a 633 nm excitation wavelength (Nd-YAG laser) with a power of 87 μW at the focal point of the sample, with a numeric aperture of 0.75. Each spectrum was recorded with 20 s exposure time and accumulated five

https://doi.org/10.1021/acsomega.2c04209
ACS Omega 2022, 7, 38674−38685

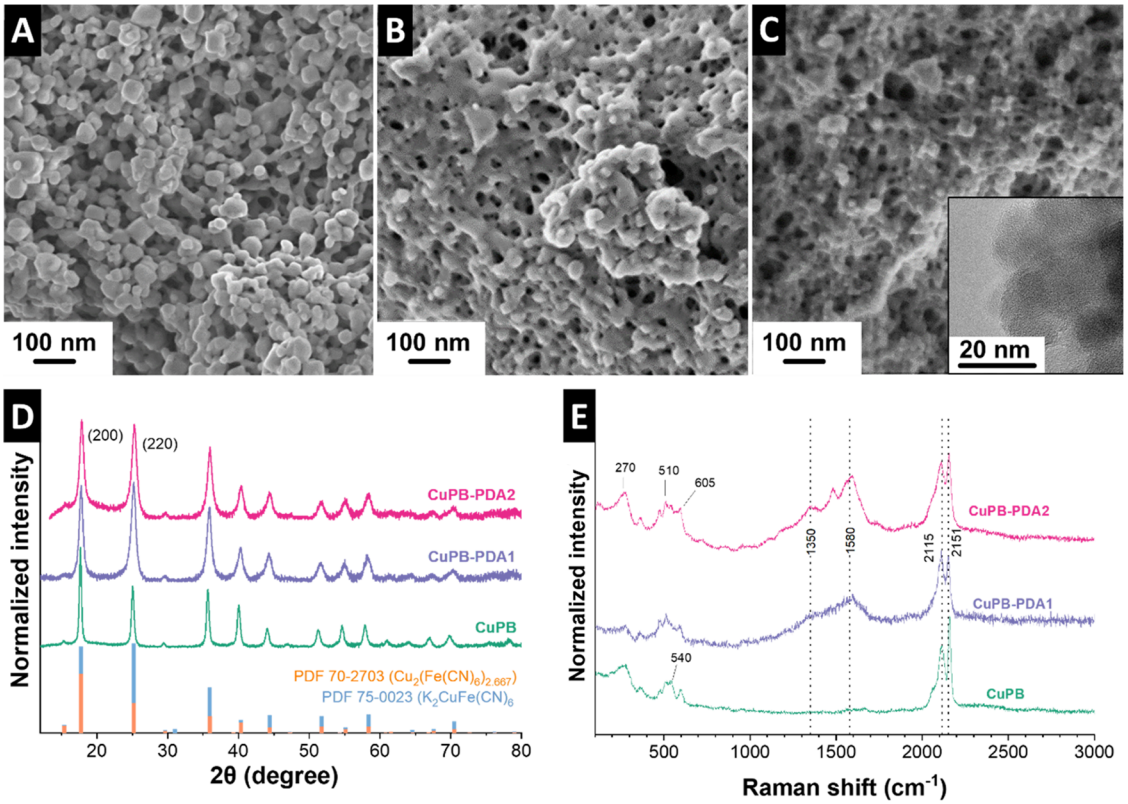

Figure 1. Scanning electron micrographs of the as-dried samples: (A) CuPB, (B) CuPB-PDA1, (C) CuPB-PDA2 (inset: transmission electron micrograph), and their respective (D) X-ray diffractograms and (E) Raman spectra.

times for each sample at least 10 points. Spectra were treated by cosmic ray removal and then normalized to (0,100).

A Netzsch TG-209-1 Libra system was used for thermogravimetric analysis (TGA) to analyze the mass changes when heating at 5 °C/min to 700 °C in synthetic air with Ar as protective gas.

2.4. Electrode Preparation. The powder material of each sample was finely ground and mixed with conductive carbon black (CB, C65, IMERYS Graphite & Carbon) and a binder poly(vinylidene fluoride) (PVDF, Sigma-Aldrich) in a mass ratio of 8:1:1. PVDF was first dissolved in *N*-methyl-2-pyrrolidone (NMP) with a mass ratio of 1:9 and stirred until it became homogeneous and then added to the mixture of the active material (AM) and conductive carbon. The consistency of the slurry was controlled by adding NMP and mixing in a speed mixer (DAC150.1 FVZ Hauschild). Initially, the dried powders of the active material and carbon black were mixed at 1000 rpm for 2 min. NMP was added in small amounts to produce a thick paste and mixed at 1000 rpm for 2 min, followed by 2500 rpm for 2 min. Then, the 10 mass % of PVDF in NMP was added to the paste and mixed at 800 rpm for 6 min. Small quantities of NMP were added and speed-mixed at 800 rpm for 2 min each time, and the consistency was checked. NMP addition continued until the mixture transitioned from the paste to a flowing viscous slurry. NMP addition was then ceased to avoid forming a runny dripping liquid. The coating was done using the doctor blade method with an automatic coater (MTI mini cast coater MSK-AFA-HC100) with a wet thickness of 200 μm onto the copper foil (MTI, 25 μm thickness). The coating was dried overnight at 110 °C in a vacuum oven and then cold press-rolled to a total thickness of 80 μm. The roll-pressed foil was punched into circles with a diameter of 10 mm to be used as the electrode. The electrodes were individually weighed with a precision of 0.01 mg. We determined the film mass using bare Cu foil. To do so, 10 punched Cu foils with a diameter of 10 mm were weighed, and the average was subtracted from the total electrode mass. The mass was normalized by the active material content (i.e., 80%), and only electrodes containing more than 1 mg of active material were used in electrochemical testing to ensure reliable measurements. The average active material mass was 1.6 ± 0.3 mg and 2.0 ± 0.1 mg for CuPB-PDA1-S and CuPB-PDA2-S, respectively.

2.5. Electrochemical Characterization. For electrochemical measurements of half-cells, CR2032 coin cells were assembled. The Cu-coated disks were used as the working electrode and a lithium chip (11 mm) as the counter and reference electrode. Whatman GF/F glass fiber mats were punched into 18 mm diameter disks and used as a separator. $LiPF_6$ salt (1 mol/L) in a mixture of ethylene carbonate and dimethyl carbonate (EC/DMC, 1:1 by volume, Sigma, battery grade) was used as the electrolyte. Cyclic voltammetry (CV) was carried out using a BioLogic VMP-300 potentiostat/galvanostat and performed in a potential window of 0.01−3.0 V vs Li/Li^+ at scan rates of 0.05 and 0.5 mV/s. Galvanostatic charge/discharge with potential limitation (GCPL) measurements were done with an Arbin Battery Cycler in the potential range of 0.01−3.0 V vs Li/Li^+ to test the rate capability and cycling stability at rates of 250, 500, and 1000 mA/g. All of the electrochemical tests were done in a Binder climate chamber held at 25 ± 1 °C.

https://doi.org/10.1021/acsomega.2c04209
ACS Omega 2022, 7, 38674−38685

Table 2. Rietveld Refinement Results of CuPB, CuPB-PDA1, and CuPB-PDA2 Were Obtained from Fitting Structures of PDF 70-2703 and PDF 75-0023

	domain size (nm)		composition ratio (mass %)	cell parameter (Å)	
	$Cu_2[Fe(CN)_6]$	$K_2Cu[Fe(CN)_6]$	$Cu_2[Fe(CN)_6]/K_2Cu[Fe(CN)_6]$	$Cu_2[Fe(CN)_6]$	$K_2Cu[Fe(CN)_6]$
CuPB1-2	26	37	44/56	10.07	10.10
CuPB1-2_PDA1	12	17	25/75	10.02	10.01
CuPB1-2_PDA2	8	10	30/70	10.03	10.02

Table 3. Elemental Analysis of CuPB, CuPB-PDA1, and CuPB-PDA2 and Their Respective Sulfidized Samples

	element (atom %)						
sample	Cu	Fe	S	K	C	N	O
CuPB	10.1 ± 0.9	5.9 ± 1.7		0.7 ± 0.2	45.3 ± 0.9	35.8 ± 2.5	2.2 ± 2.5
CuPB-PDA1	9.2 ± 1.1	6.8 ± 2.3		5.7 ± 1.8	44.4 ± 2.0	30.5 ± 3.0	3.3 ± 0.6
CuPB-PDA2	7.4 ± 0.4	3.3 ± 0.4		2.4 ± 0.3	49.1 ± 0.4	32.0 ± 1.4	5.8 ± 0.2
CuPB-S	12.8 ± 2.6	41.8 ± 8.13	30.0 ± 3.1	1.9 ± 0.4	11.1 ± 3.9	0.2 ± 0.4	2.1 ± 0.5
CuPB-PDA1-S	24.7 ± 2.1	8.9 ± 0.8	23.1 ± 1.7	5.7 ± 1.4	32.4 ± 2.7	2.3 ± 0.7	3.0 ± 0.3
CuPB-PDA2-S	11.8 ± 1.3	6.1 ± 1.2	14.3 ± 2.6	4.2 ± 0.8	40.9 ± 4.6	5.3 ± 0.8	17.4 ± 3.4

3. RESULTS AND DISCUSSION

3.1. Synthesis of CuPB Using Dopamine. CuPB was prepared by coprecipitation, a well-established and straightforward method for synthesizing PB and PBA nanoparticles.[12] Ming et al. reported that the pH of the synthesis solution and the concentration of the precursor salts directly affect the morphology and the particle size. A defect-free structure has been shown to enhance the energy storage ability[31] and is preferred here as a more homogeneous template for further derivatization. The 1:2 Cu/Fe ratio was employed to minimize introduced defects by a lack of cyanide ligands in the synthesis.[34]

After adding the copper salt to the ferricyanide, a dark brown opaque solution was formed. In the synthesis of PDA-coated samples, dopamine hydrochloride was first dissolved in the ferricyanide solution prior to the addition of $CuCl_2$. When adding the dopamine, the color of the solution changed from the characteristic bright yellow of $[Fe(CN)_6]^{3-}$ to deep red, which is assigned to the oxidation of dopamine by ferricyanide and reduction of Fe^{3+} to Fe^{2+}. The color difference between the batches with and without dopamine is shown in Figure S1A,B, Supporting Information.

The morphology of the produced powders was studied by SEM (Figure 1). A higher amount of PDA in the solution has a visible effect on the morphology, namely, the connectivity increases among the PBA particles, and there is a general reduction in the particle size (Figure 1A−C). The particle size distribution was calculated by measuring the diameter of 100 particles of each sample from scanning electron micrographs resulting in an average particle size 24 ± 0.3 and 22 ± 0.6 nm for CuPB-PDA1, and CuPB-PDA2, respectively (Figure S1C). In the absence of dopamine or any protecting agent, PB particles present progressive nucleation, that is concomitant nucleation and growth, resulting in heterogeneous particle size distribution.[35] Due to less control over the nucleation and growth in the CuPB, a bimodal size distribution is observed, resulting in centers of 26 ± 0.6 and 43 ± 8 nm. The TEM inset in Figure 1C demonstrates the CuPB-PDA2 particles smaller than 20 nm and the amorphous PDA coating around them. These observations and the color change in the presence of dopamine indicate direct participation of PDA in the synthesis procedure, which is related to the dopamine polymerization process. PDA is formed through the oxidative polymerization of dopamine. Therefore, a key step for PDA synthesis is the oxidation of dopamine, which commonly occurs in an alkaline environment and/or in the presence of an oxidizing agent.[36] Previous works have mentioned that one or both conditions are necessary for dopamine molecules to be activated through the deprotonation of the hydroxyl group and self-polymerize.[37,38]

In the presence of transition metals, especially Fe^{3+}, the hydroxyl groups of catechols can chelate to the metal species, forming a reversible noncovalent complex by donating a pair of nonbonding electron pairs to the iron ion. This results in the formation of mono- to tris-catechol-metal ion complexes depending on the concentration of Fe^{3+} [39,40] and the pH.[41] Here, the ferricyanide ion can act as a mild oxidizing agent through coordination and electron transfer from dopamine. The reduced $[Fe(CN)_6]^{4-}$ ions act as nucleation sites for PBA particle growth when the copper salt is added to the solution. The presence of oxidized dopamine around $[Fe(CN)_6]^{4-}$ increases the distance between the nucleation sites, impedes particle growth, and results in smaller particles.

X-ray diffractograms of the produced samples are presented in Figure 1D. The diffractograms feature the characteristic reflections of a PB(A) cubic structure, matching both $Cu_2[Fe(CN)_6]$ and $K_2Cu[Fe(CN)_6]$ phases with a cubic system and space group of $Fm\bar{3}m$ (225) and $F\bar{4}3m$ (216), respectively. The samples containing PDA showed a higher (220) peak intensity than the (200) peak, indicating a possible better match with the K-rich phase. The uncoated CuPB sample also displays narrower peaks than the PDA-coated material, suggesting a larger particle size. These observations were further analyzed by Rietveld refinement (Table 2 and Figure S2). The Rietveld refinement reveals that all samples present a mixture of $Cu_2[Fe(CN)_6]$ and $K_2Cu[Fe(CN)_6]$, with the PDA-containing samples showing more of the K-rich phase. The amount of K-CuPB increased from 56% in CuPB to 75% and 70% in CuPB-PDA1 and CuPB-PDA2, respectively. The overall domain size of the CuPB material also tends to be larger than the other two. This aligns with the larger particles in scanning electron micrographs (Figures 1A and S1C). After the PDA addition, the crystallite size of both phases decreases significantly from 37 nm for $K_2Cu[Fe(CN)_6]$ in the CuPB sample to 17 and 10 nm in CuPB-PDA1 and CuPB-PDA2, and

https://doi.org/10.1021/acsomega.2c04209
ACS Omega 2022, 7, 38674−38685

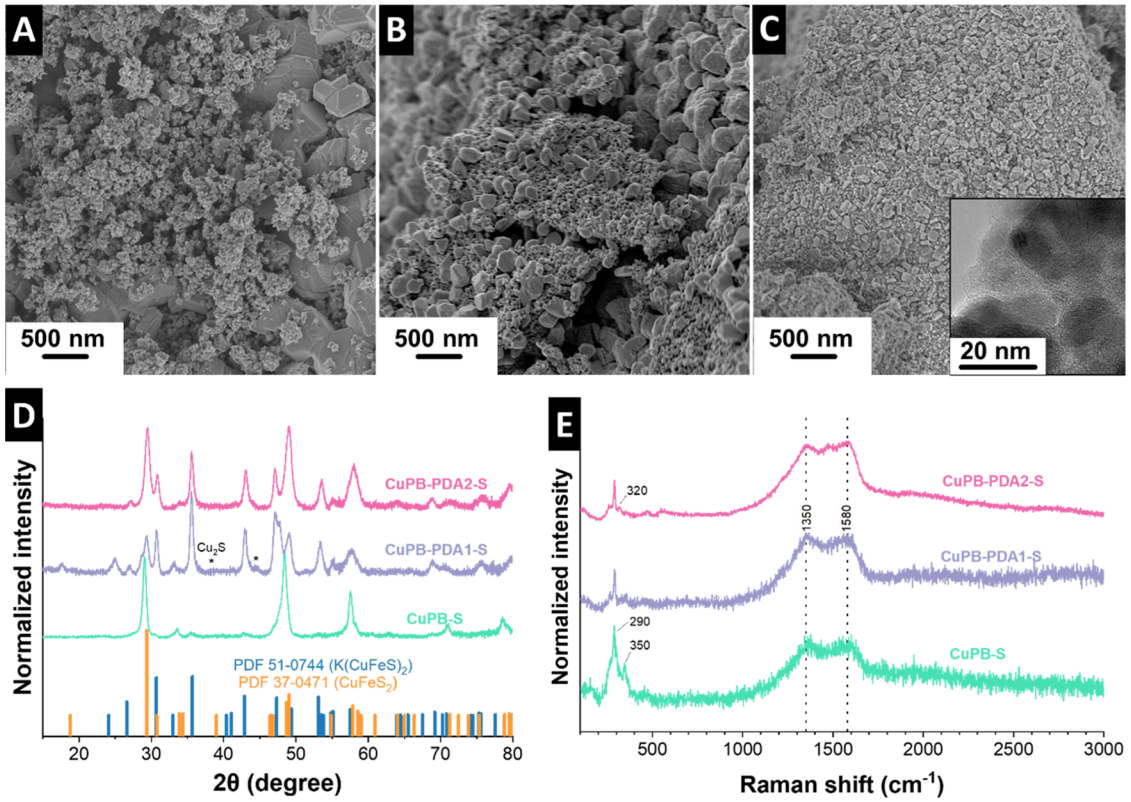

Figure 2. Scanning electron micrographs of the sulfidized sample: (A) CuPB-S, (B) CuPB-PDA1-S, (C) CuPB-PDA2-S (inset: transmission electron micrograph) and their respective (D) X-ray diffractograms and (E) Raman spectra.

for $Cu[Fe(CN)_6]$, from 26 to 12 and 8 nm, respectively. This trend confirms the dopamine effect surrounding the $[Fe(CN)_6]^{3-}$ ions during synthesis and controlling the particle size in both present phases.

The composition of the samples was further analyzed by energy-dispersive X-ray spectroscopy (Table 3). Analysis of the samples identified the following elements: copper, iron, potassium, carbon, nitrogen, and oxygen. In both samples with PDA, more potassium is observed (5.7 atom % in CuPB-PDA1 and 2.4 atom % in CuPB-PDA2), supporting the higher $K_2Cu[Fe(CN)_6]$ phase content in these samples, while in the sample with no PDA, a very low amount of potassium was detected (0.7 atom %). This confirms that during the synthesis, the reduction of ferricyanide ions to $[Fe(CN)_6]^{4-}$ favors the interaction of potassium ions for charge balance. The alkali-rich phase of PB materials is known to be less defective and more electrochemically stable. This PDA-induced effect could not only be used to produce more stable structures but also to incorporate other countercations like Li^+, which could compensate for Li consumption during solid-electrolyte interphase (SEI) formation, for example. Detected potassium was higher in the CuPB-PDA1 sample but with a larger deviation, probably due to the lower homogeneity compared to the CuPB-PDA2 sample. The thicker PDA coating in CuPB-PDA2 also diminishes the signal intensity of CuPB-related components. Therefore, no straight relation between the coating thickness and potassium amount was concluded. Other elements present in the PDA molecule (carbon, nitrogen, and oxygen) slightly increased in the PDA-containing samples. The main change was the increase of oxygen from 2.2 atom % in CuPB to 5.8 atom % in CuPB-PDA2, while carbon went from 45.3 to 49.1 atom % in the same samples.

Figure 1E shows the Raman spectra of the samples before the derivatization. The set of bands from 200 to 700 cm^{-1} belong to the Fe−CN−Cu vibrations due to M−CN−M′ bonds.[42] Two bands at ∼2115 and ∼2151 cm^{-1} correspond to A_{1g} and E_{1g} modes of ν(CN) vibrations, respectively. The high-frequency one is usually associated with inner sphere metal species coordination (NC−M), in this case, Fe ions, due to stronger bond and π back-bonding effects. At the same time, the lower frequency corresponds to M′−NC effects.[43] The increase in the low-frequency mode after the PDA addition indicates the higher contribution of Cu−NC, which is associated with a less defective structure due to more Cu units.[44] In the presence of dopamine, the D-band and G-band of carbon are seen at 1350 and 1580 cm^{-1}, respectively, and we see further growth of the carbon signal with higher dopamine addition. The band at 1480 cm^{-1} between the D-band and the G-band appears with increased dopamine content and shows the functional groups in the PDA (e.g., −OH scissoring).[45] TGA analysis (Figure S3A, Supporting Information) confirms the presence of the carbon species by the difference in the mass loss between CuPB and CuPB-PDA2, indicating that approximately 10 mass % of the coated sample is carbon coating contribution.

3.2. Sulfidation of Cu-PB. The samples were further treated under H_2S to achieve mixed metal sulfide, resulting in the morphologies shown by scanning electron micrographs in Figure 2A−C. The sulfidation process was optimized to ensure total conversion of the CuPB precursor while avoiding particle growth. Figure 2D presents the X-ray diffractograms of the treated samples. All samples were fully sulfidized at 300 °C after 10 min, as phase analysis shows that no remaining peaks from the PBA precursor are apparent. The resulting powder is

https://doi.org/10.1021/acsomega.2c04209
ACS Omega 2022, 7, 38674−38685

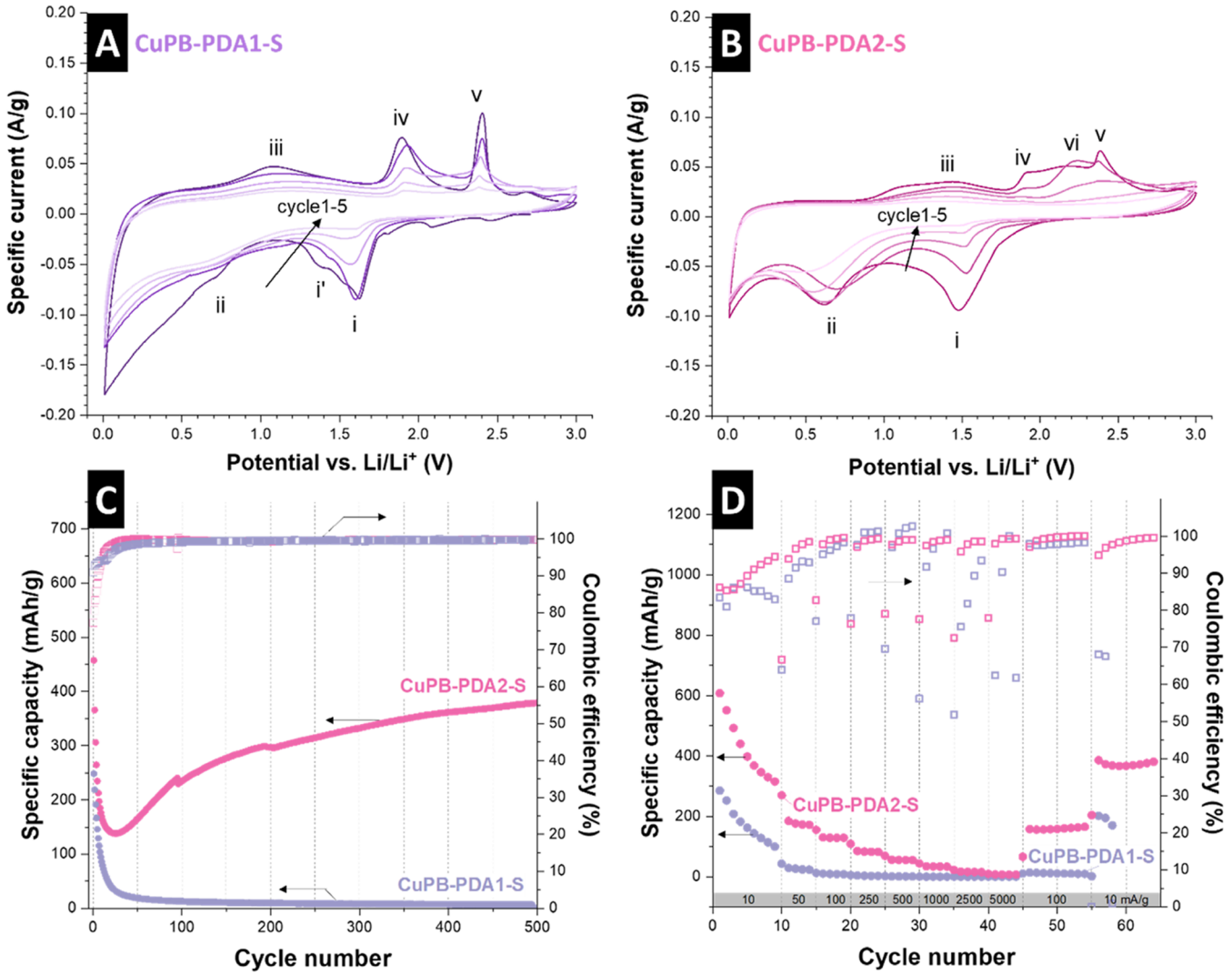

Figure 3. Cyclic voltammetry of (A) CuPB-PDA1-S and (B) CuPB-PDA2-S at 0.05 mV/s. (C) Cycling stability of CuPb-PDA1-S and CuPB-PDA2-S under a current rate of 250 mA/g. (D) Rate handling performance of CuPB-PDA1-S and CuPB-PDA2-S at different rates.

a crystalline mixed sulfide material. In the CuPB sample, the main peaks are attributed to tetragonal copper-iron sulfide ($CuFeS_2$) with the space group of $I\bar{4}2d$ (122) and a c/a unit cell ratio of 1.97, which indicates lattice expansion after the sulfidation. This phase change can significantly affect the structure, resulting in an inhomogeneous structure despite the short treatment time, as seen in the scanning electron micrographs (Figure 2A,B). There is a significant change in the product's composition when CuPB is coated with PDA. The new reflections correspond to the $KCuFeS_2$ phase (Figures 2D and S4). This observation confirms the previous characterization data, indicating the stabilization of potassium in the structure after adding the PDA to the PBA solution and its preservation in the structure after derivatization.

The presence and the amount of polydopamine affect the final derived sulfide composition. In the CuPB-PDA1-S sample, minor reflections other than those of tetragonal $CuFeS_2$ and $KCuFeS_2$ were indexed with CuS_x (Figure 2D), whereas the CuPB-PDA2-S sample only showed peaks conforming to $CuFeS_2$ and $KCuFeS_2$. The more homogeneous phase structure in CuPB-PDA2-S can be due to a thicker polymer coating and, therefore, slower diffusion of sulfur in the material and a more controlled derivatization and phase formation.

The initial sulfidized sample CuPB-S showed the largest particle size and morphology inhomogeneity, with particle size ranging from ~20 nm to 1 μm (Figure 2A). The derivatization process was more controlled and resulted in a more homogeneous structure upon the PDA addition. While large particles with micrometer range size and, at some parts, cracks were observed in CuPB-S and CuPB-PDA1-S (Figure S5A,B in Supporting Information), the morphology of the sample CuPB-PDA2-S showed better homogeneity and a consistent structure with a uniform sub-100 nm particle size (Figure 2C). This could be assigned to both the presence of a thicker PDA coating that prevents not only particle aggregation but also the characteristics of the CuPB precursor. Previous works on PB(A) synthesis[36,46,47] show that the presence of defects, which is usually a result of insufficient cyanide bridging, changes the structure of the lattice from cubic and monoclinic and that this structure change is accompanied by the presence of water molecules in the lattice (referred as insoluble PB, even though is not related to its solubility). However, when alkali ions instead of water molecules are stabilized in the lattice (soluble PB), the formation of vacancies is suppressed, and a

https://doi.org/10.1021/acsomega.2c04209
ACS Omega 2022, 7, 38674−38685

lower defect-containing structure is formed. As the CuPB particle acts as a template and metallic source for the produced sulfides, the lower defect degree in the parent material aids in the homogeneity of the final product.

In the transmission electron micrographs shown in Figure 2C inset and Figure S5C,D, Supporting Information, the particles' crystallinity is confirmed, with a *d*-spacing of 0.301 nm, matching the (111) planes of the tetragonal $CuFeS_2$ phase at ∼29.5° 2θ shown in Figure 2D. An amorphous carbon coating is also observed around the particles, indicating the successful employment of the PDA as a carbon shell precursor. This confirms that the coating amount controls the morphology and growth rate of the sulfide particles, leading to higher homogeneity of the resulting derivative.

In addition to the structure, chemical heterogeneity was also observed via EDX elemental analysis (Table 3). The potassium content remained with a similar trend within the samples. After the heat treatment, the nitrogen amount decreased in all samples from ∼30 to 5 atom % or below, which shows the nitrogen removal from the cyanide ligand. Carbon was also reduced but in less extent, retaining ∼11, 32, and 41 atom % for CuPB-S, CuPB-PDA1-S, and CuPB-PDA2-S, respectively, which demonstrates a thicker coating in the CuPB-PDA2-S sample. After the sulfidation, the mean and standard deviation of iron in CuPB-S indicates an inhomogeneous structure. With PDA addition, more homogeneity in the chemical composition can be observed with a lower deviation in the spectrum values and a higher carbon content due to the thicker coating. The mass reduction of the PDA can explain the sensitivity of the material homogeneity to the PDA coating amount during the heat treatment due to the conversion of the intermediates in PDA.[48] If the polymer does not thoroughly coat the substrate or is lost during the heat treatment, it weakens the diffusion barrier. It causes overgrowth of sulfide particles where no enough coating covers the material, resulting in morphological and chemical heterogeneity. The presence of oxygen with 17.4 atom % in CuPB-PDA2-S can indicate the incomplete transformation of PDA to carbon.

Raman spectra of the heat-treated samples are shown in Figure 2E. The bands at lower frequencies of 200−500 cm^{-1} belong to the metal sulfide at ∼290, 320, and 350 cm^{-1}, corresponding to the A_1, B_2, and E_g modes of chalcopyrite metal-sulfur vibrations, respectively.[49−51] The D-mode and G-mode related to carbon bands from the sp^3 and sp^2 C−C bonding at 1350 and 1580 cm^{-1}, respectively, present narrowing after the thermal treatment, reflecting higher crystallinity of carbon as a result of the PDA heat treatment. In the CuPB-PDA2-S sample, the third band at ∼1480 cm^{-1} is still present, indicating that PDA intermediates do not fully transform into carbon, which is expected from the low heat treatment temperature and duration. TGA of the sulfidized samples without coating CuPB-S and with more coating CuPB-PDA2-S is shown in Figure S3B, Supporting Information. Similar mass change events occur at lower temperatures for CuPB-S compared to CuPB-PDA2-S, showing its higher sensitive for oxidation by the atmosphere and PDA protective effect. For CuPB-PDA2-S, the mass loss before 450 °C and the lower mass increase after 450 °C are due to the burning of the coating by oxygen. The coating also protects the sulfide particles from oxidation, and therefore, the mass increase and oxidation peaks are delayed in the latter sample, taking place at higher temperatures.

3.3. Electrochemical Performance as Li-Ion Battery Electrode. The electrochemical behavior of CuPB-PDA1 and CuPB-PDA2 electrodes operated as half-cells was explored for application in lithium-ion batteries. Figure 3A,B shows cyclic voltammetry of CuPB-PDA1-S and CuPB-PDA2-S, respectively. The voltammogram in Figure 3A shows three main reduction peaks at 1.60 V vs Li/Li^+ (i), 1.38 V vs Li/Li^+ (i′), and 0.68 V vs Li/Li^+ (ii). Through the anodic sweep, three peaks are observed at 1.09, 1.92, 2.40 V vs Li/Li^+ denoted as iii, iv, and v, respectively. The voltammogram of CuPB-PDA2-S (Figure 3B) shows reduction peaks at ca. 1.5 V vs Li/Li^+ (i) and ca. 0.6 V vs Li/Li^+ (ii). At the anodic sweep, the first cycle presents similar oxidation peaks at 1.45 V (iii), 1.90 V (iv), and 2.45 V (v) vs Li/Li^+ and an additional peak at 2.22 V (vi). The latest two further broaden and merge, while all processes decay in intensity upon cycling. This profile is a combination of processes observed for Cu_2S and FeS_2, given the overall behavior of $CuFeS_2$. The mechanism of charge storage in $CuFeS_2$ starts with the intercalation of Li^+ upon iron reduction, which is accompanied by a cathodic peak at ca. 1.65 V vs Li/Li^+ [52]

$$CuFeS_2 + Li^+ + e^- \rightarrow LiCuFeS_2 \quad (1)$$

For the $KCuFeS_2$ phase, lithiation takes place by replacing potassium ions, forming $Li_xK_{1-x}CuFeS_2$.[53,54] In the same potential range, the reduction and formation of metallic copper occur at ca. 1.5 V vs Li/Li^+ [55]

$$LiCuFeS_2 + Li^+ + e^- \rightarrow Cu^0 + Li_2FeS_2 \quad (2)$$

As we have $CuFeS_2$ and $KCuFeS_2$ phases in the samples, the broad reduction process between 1.75 and 1.25 V vs Li/Li^+ can be assigned to the lithiation of $CuFeS_2$ and copper reduction of both phases. The subsequent conversion stage, which is accompanied by a broad peak from 0.8 to 0.5 V vs Li/Li^+ is well in line with the SEI formation and reduction of Fe, which results in eq 3

$$Li_2FeS_2 + 2e^- + 2Li^+ \rightarrow Fe^0 + 2Li_2S \quad (3)$$

Similarly, the first broad oxidation process (peak iii in both CuPB-PDA1-S and CuPB-PDA2-S) refers to the partial oxidation of iron to Fe^{2+} in Li_2FeS_2, followed by the peak at 1.90 V vs Li/Li^+ due to conversion of Cu into Cu_2S. The processes above 2.0 V vs Li/Li^+ relate to further delithiation of the Li_2FeS_2 species and partial oxidation of sulfur.[53] While the conversion of Cu is quite reversible, the iron species do not fully oxidize back at 3.0 V vs Li/Li^+, indicating the presence of irreversible mechanisms.[55] A summary of the possible redox reactions for the $CuFeS_2$ system is presented in Table S1, Supporting Information.[15,53,55,56]

Figure 3C shows the cycling stability of the samples at 250 mA/g. The capacity of CuPB-PDA1-S starts at 248 mAh/g and fades quickly after about 20 cycles. This is typical for sulfide materials when tested over an extended voltage window to potentials lower than 1.2 V vs Li/Li^+.[53] Capacity fading occurs after a few cycles due to the volume expansion and disintegration of the material during the conversion reactions and shuttling of polysulfides. While coating of the particles is a common strategy to buffer expansion and limit the diffusion of polysulfides, the quality of coating and its homogeneity directly affect the performance.[57−59] This is demonstrated by the significant improvement of long-term cycling of the sample CuPB-PDA2-S. An initial capacity decay is observed in the

https://doi.org/10.1021/acsomega.2c04209
ACS Omega 2022, 7, 38674−38685

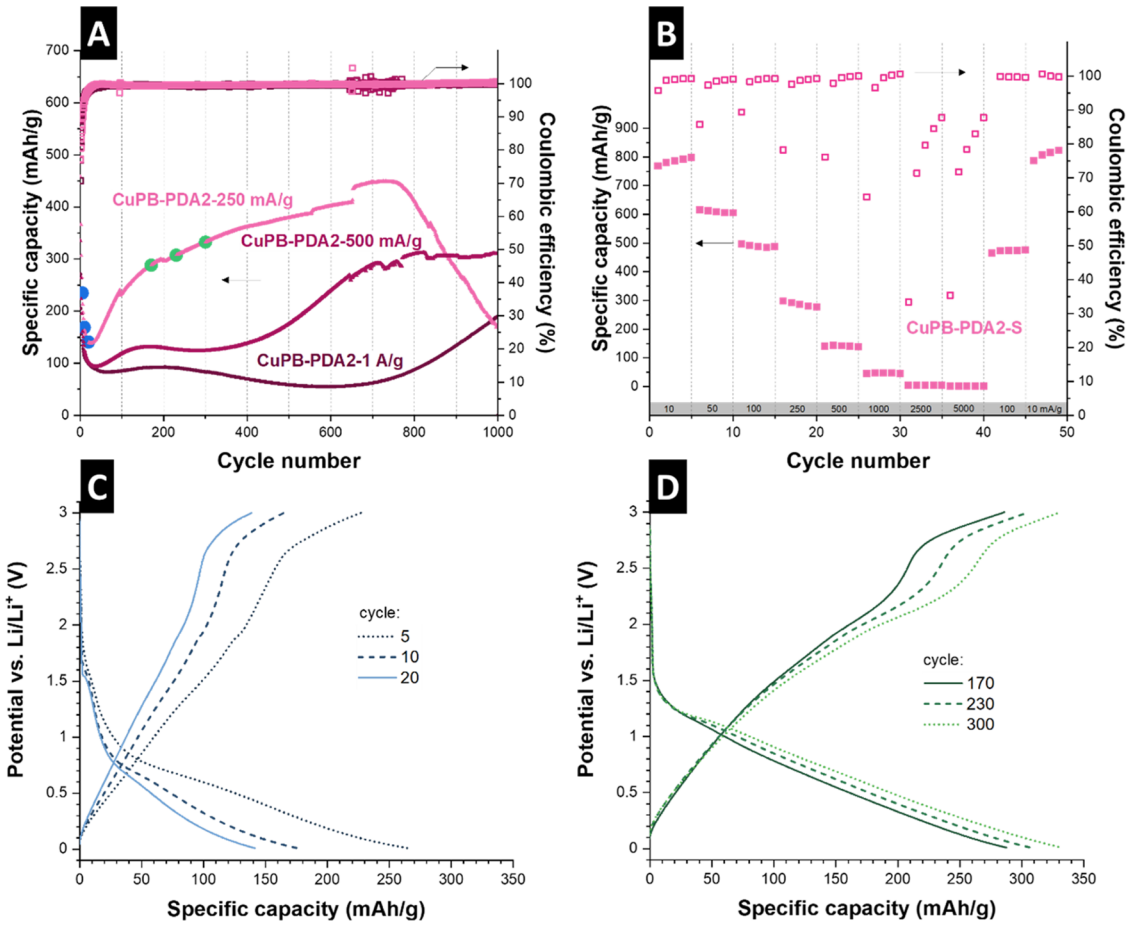

Figure 4. (A) Specific discharge capacity of CuPB-PDA2-S at 250, 500, and 1000 mA/g. (B) Rate handling of CuPB-PDA-S at 250 mA/g after 500 cycles. (C, D) Galvanostatic charge and discharge curves of CuPB-PDA2-S from the chosen points in panel (A).

sample, starting from ~460 mAh/g and decreasing to ~150 mAh/g after 25 cycles. However, it then gradually increases to ~400 mAh/g. First, this demonstrates that the amount of the coating material directly affects the derivative performance. Nevertheless, it shows that the C-coated sulfide material requires activation to achieve its full capacity.

The Coulombic efficiency for CuPB-PDA2-S starts at ca. 80%, quickly rising above 95% in the first 25 cycles, corresponding to the initial capacity decay of this sample. This indicates the occurrence of irreversible reactions likely related to FeS_2 species as well as SEI formation. Nevertheless, further cycling presents steady Coulombic efficiencies in the range of 97−100%, which shows that the constant increase in capacity is possibly an activation process rather than phase transformations.[56] Figure 3D displays the discharge performance at different applied rates for CuPB-PDA1-S and CuPB-PDA2-S. At 0.01 A/g, CuPB-PDA2-S presents 607 mAh/g, which is higher than the reported theoretical capacity of 583 mAh/g for $CuFeS_2$.[60] This theoretical capacity is based on the four-electron process of iron and copper reduction. However, at the applied potential range, sulfur species also undergo reactions with lithium, contributing to the total capacity (Table S1, Supporting Information). Furthermore, the contribution of the carbon coating cannot be completely ignored, though the capacity from carbon should be limited due to the low graphitization degree. The initial capacity of CuPB-PDA1-S at 0.01 A/g is 285 mAh/g, less than half of CuPB-PDA2-S. This could be due to a more inhomogeneous structure both in morphology and composition and the much larger particle size, leading to a less exposed surface area, as previously observed by scanning electron microscopy (Figure 2B).

The capacity of CuPB-PDA1-S is nearly zero at higher rates, except for the recovered ~200 mAh/g at the rate of 0.01 mA/g. With a thicker coating, CuPB-PDA2-S can deliver 200 mAh/g (0.50 A/g), 180 mAh/g (0.10 A/g), and 100 mAh/g (1.0 A/g). After cycling at higher rates for 40 cycles, the electrodes yield a residual capacity of 150 mA/g at 0.10 A/g and 380 mAh/g at 0.01 A/g. The combined characteristics of CuPB-PDA2-S help the material perform better as it has a smaller particle size, a higher amount of carbon for conductivity and connectivity, and a thicker carbon coating that provides mechanical stability under volumetric changes. Nevertheless, the overall performance is lower than expected for these mixed Cu and Fe sulfides. Similar to what is observed in the stability test, there is a fast capacity drop together with low Coulombic efficiency in the initial cycling.

To understand the behavior of CuPB-PDA2-S under cycling, stability tests were conducted at a rate of 500 mA/g and 1 A/g (Figure 4A). Cycling at higher rates showed that the increase in the capacity takes place in two steps that occur at larger intervals when tested at a faster rate. The first step of capacity increase finishes in the first 200 cycles, and its duration is less affected by the current rate. This is probably due to the carbon coating activation. Since no conditioning was done before the tests, the coating is not well-tailored for the diffusion of Li^+ ions. After multiple cycling, more pores are opened, the more

https://doi.org/10.1021/acsomega.2c04209
ACS Omega 2022, 7, 38674−38685

Table 4. Performance Data of Copper and Iron Mixed and Unmixed Sulfide Electrodes for Li-Ion Batteries[a]

active material	electrode composition	electrolyte	potential window (V vs Li/Li^+)	capacity values at different rates	reference
$KCuFeS_2/CuFeS_2$ nanoparticles	AM/CB/PVDF 8:1:1	1 M $LiPF_6$ EC/DMC	0.01−3.0	798 mAh/g at 0.01 A/g	this work
$CuFeS_2$ nanorods	AM/acetylene black/PVDF 7:1.5:1.5	1 M $LiPF_6$ EC/DMC/DEC	1.0−3.0	633 mAh/g at 0.2 C	15
	AM/acetylene black/PVDF 7:1.5:1	DOL/DME	1.0−3.0	675 mAh/g at 0.2 C	15
$CuFeS_2$ quantum dots/carbon frame	AM/CB/PVDF 7:2:1	1 M $LiPF_6$ EC/DMC	0.005−3.0	1150 mAh/g at 0.05 A/g	56
Natural chalcopyrite	AM/CB/CMC 7:1.5:1.5	1 M $LiPF_6$ EC/DMC/DEC	0.01−3.0	990 mAh/g at 1 A/g	53
	AM/CB/sodium alginate 7:1.5:1.5	1 M $LiPF_6$ EC/DMC	0.01−3.0	1010 mAh/g at 1 A/g	63
FeS_2-CNT	AM/carbon/PVDF 8:1:1	1 M LiTFSI DGE	1.0−3.0	695 mAh/g at 1 A/g	68
Cu_2S	AM/CB/PVDF 7:1.5:1.5	1 M $LiPF_6$ in EMC	1.0−3.0	243 mAh/g at 0.5 C	67

[a]AM = active material, CB: carbon black, EC: ethylene carbonate, DMC: dimethyl carbonate, DEC: diethyl carbonate DOL: 1, 3-dioxolane, DME: dimethyl ether, LiTFSI: lithium bis(trifluoromethanesulfonyl)imide, DGE: diethylene glycol dimethyl ether.

surface area is available to the ions, and diffusion takes place easier.[13] It was previously demonstrated that the thickness and homogeneity of the coating significantly affect charge storage capacity and rate handling.[59,61] Therefore, there is an optimal thickness to achieve the best electrochemical performance. While the thinner coating does not provide enough conductivity and mechanical stability, thicker coatings can limit Li^+ diffusion through the active material, presenting decreased capacity and sluggish kinetics.

The second increase in the capacity starts after a different number of cycles depending on the current rate. When testing at 250 mA/g, the second increase is merged with the carbon activation and cannot be well defined. However, by increasing the current rate, the process is inhibited and can be well distinguished from the first step.

Several points were chosen from the stability curves at different rates (marked with different colors) to compare their charge and discharge profile (Figure S6, Supporting Information). The initial 5, 10, and 20 cycles from the current rate of 250 mA/g are shown in Figure 4C. All curves presented a similar profile during lithiation with a short plateau at ca. 1.5 V vs Li/Li^+, and a second plateau starting at 0.75 V vs Li/Li^+ extends to a long slope, referring to peaks (i) and (ii), respectively, previously observed in cyclic voltammetry (Figure 3B). The charge profile is characterized by a long slope from 0.01 to 2.0 V and a second slope from 2.5 to 3.0 V vs Li/Li^+. The main difference between the tested rates is in the extent of the plateaus related to the conversion reactions, indicating that the material cannot be fully lithiated at higher rates.

After continuous cycling, the discharge profile changed in all of the rates, which indicates the change in the lithiation mechanism. The evolution of the new behavior was observed earlier in the sample cycled at 250 mA/g, already from the 160th cycle, and was accompanied by the formation of a new plateau at ∼1.25 V vs Li/Li^+ followed by a slope (Figure 4D). At this stage, a large portion of the capacity is recovered. Further charge/discharge curves at 250 mA/g showed the same profile with increased contribution of the 1.25 V plateau and the following slope, which leads to the capacity increase in the stability test.

For the material tested under 500 mA/g, the aforementioned transition occurs at later cycles (Figure S6, Supporting Information). Although the first changes and plateau formation at ∼1.25 V vs Li/Li^+ can be seen at the onset of the 160th cycle, it is after 400 cycles that this process is intensified, leading to an increase in the capacity as observed in the profile of the 500th cycle. However, the processes are not fully stabilized, and both the plateau and the slope after it show a continuous increase in capacity. The same behavior occurs at 1 A/g, with the first profile change visible in the 160th cycle. At this rate, the material takes even more cycles to undergo the reaction with a plateau at 1.25 V vs Li/Li^+, which is strong evidence of the reaction's dependence on diffusion.

Similar phenomena were previously described for $CuFeS_2$ and CuS species,[62,63] where the capacity increase occurs after continuous cycling. Even though the charge storage mechanism of $CuFeS_2$ is usually described as a combination of lithiation of the mixed sulfide and further conversion reactions, the Cu−S system is much more complex, with several nonstoichiometric Cu_xS_y intermediates. Rate handling was done after 500 cycles at 250 mA/g to compare the rate handling of the material after its activation (Figure 4B). The behavior of the capacity changed drastically compared to that previously observed in Figure 3D. The initial capacity at 10 mA/g increased to 770 and 490 mAh/g at 100 mA/g. After cycling at higher rates, 790 and 470 mAh/g were recovered at those rates. As discussed previously, the theoretical capacity of $CuFeS_2$ is 587 mAh/g, while we find 438−587 mAh/g for K_xCuFeS_2 ($x \leq 1$). Higher capacities are normally described for $CuFeS_2$ and assigned to a transition from the Li−$CuFeS_2$ system to a combination of Li−FeS_2, LiFeS, Li−Cu_2S, and Li−S as described in the reactions of Table S1, Supporting Information.[53,63]

The postmortem X-ray diffraction analysis of the cycled cells (Figure S7A, Supporting Information) showed that sharp peaks of elemental copper appear after the second capacity increase, and its amount increases upon more cycling. Since the postmortem XRD of the electrodes was done on the powder removed from the current collector, the observed copper peak arises from the sample. The presence of elemental copper has been reported to act as a polysulfide capturing agent,[64,65] which prevents $CuFeS_2$ from enduring rapid capacity fading due to a polysulfide shuttling. Since copper is highly mobile and its diffusion in $CuFeS_2$ required less activation energy compared to Fe and K at room temperature,[53,66] Cu leaves the lattice during lithiation, resulting in the formation of $LiFeS_2$ and metallic Cu.[54] Upon cycling, Cu_xS_y species are formed that can again reduce to Cu and Li_2S, generating the observed plateau at 1.25 V vs Li/Li^+.[57] It is described that the reduction mechanism of Cu_2S to metallic

https://doi.org/10.1021/acsomega.2c04209
ACS Omega 2022, 7, 38674−38685

copper occurs through a displacement process, where copper is extruded from the formed Li_2S crystals and needs to diffuse through the particle.[67] Therefore, all of the processes involving the reduction of Cu-containing species depend on Cu diffusion. The need for Cu diffusion and phase conversion during cycling explains the lagging performance at higher rates. This can also explain the capacity increase upon continuous cycling, in which the carbon layer is slowly activated enabling faster charge mobility necessary for the conversion reactions.

Postmortem scanning electron micrographs (Figure S7B,C, Supporting Information) did not show any changes in the morphology of the active material or dissociation of the particles. This indicates that the conversion reactions do not lead to particle disruption or aggregation. This could be a reason for the increased capacity and stability in the rate handling after activation. Furthermore, the carbon coating and the small particle size contribute to the structure stability by limiting the volume expansion.

We see a significant influence of the PDA coating on electrochemical performance. A higher amount of coating enabled the material to activate through reversible conversion reactions and reach a stable capacity after the rate test. The summary of the results in this work is presented and compared with similar works in the literature in Table 4. Our results are comparable with synthetic nano $CuFeS_2$ works and demonstrate higher achieved capacities while using a more scalable and quicker synthesis procedure. Although we prepared the material by a facile method and showed a high-capacity recovery after the rate handling, the performance at higher rates is hindered due to limited diffusion possibly as a result of C-coating properties. The conductivity within the particles could be further improved by increasing the graphitization degree of the carbon coating or utilizing different carbon additives, while an intermediate coating thickness could help in the diffusion, enhancing the performance at higher rates.

4. CONCLUSIONS

Copper Prussian blue analogue (CuPBA) was synthesized in the presence of dopamine and used as a template to prepare carbon-coated mixed Cu−Fe sulfides. Dopamine alters the synthesis of CuPB through its oxidative polymerization process by reducing the ferricyanide precursor, favoring K-rich CuPB, and controlling the particle size by steric effects and formation of dopamine−Fe complex Thus, PDA-coated CuPB particles are less defective and more homogeneous compared to bare CuPB. While the sole presence of PDA translates into a more K-rich phase, its quantity determines coating thickness. These two effects are correlated and cannot be disassociated. The material was thermally sulfidized under fast and mild conditions, producing homogeneous C-coated $KCuFeS_2$ nanoparticles. It was shown that the thickness of the coating is of great importance for the stable electrochemical performance of the iron−copper mixed-metal sulfide as the LIB electrode. At the same time, the thicker coating requires activation of the carbon layer to achieve higher capacity and better rate handling. During cycling, $CuFeS_2$ is gradually reduced to metallic copper and iron, resulting in the combination of redox processes of iron sulfide, copper sulfide, and lithium sulfide species. The presence of elemental copper and carbon coating impedes the shuttling of polysulfides during cycling. The material presents a diffusion-controlled activation process, with a capacity increase from 300 to 400 mAh/g at 250 mA/g, reaching 800 mAh/g at 10 mA/g. After activation of 500 cycles, the rate handling showed excellent capacity recovery and stability. The effect of PDA can impact future derivatization works on PB/PBA through their morphology and phase control.

■ ASSOCIATED CONTENT

Data Availability Statement

The data can be made available upon request.

Supporting Information

The Supporting Information is available free of charge at https://pubs.acs.org/doi/10.1021/acsomega.2c04209.

Material characterization of PDA-coated CuFe Prussian blue particles before and after sulfidation by Rietveld refinement and thermogravimetric analysis; additional transmission electron micrographs; and comprehensive electrochemistry data and its postmortem analysis for the sample CuPB-PDA2-S (PDF)

■ AUTHOR INFORMATION

Corresponding Authors

Volker Presser − *INM—Leibniz Institute for New Materials, 66123 Saarbrücken, Germany; Department of Materials Science & Engineering, Saarland University, 66123 Saarbrücken, Germany; Saarene—Saarland Center for Energy Materials and Sustainability, 66123 Saarbrücken, Germany;* orcid.org/0000-0003-2181-0590; Email: volker.presser@leibniz-inm.de

Samantha Husmann − *INM—Leibniz Institute for New Materials, 66123 Saarbrücken, Germany;* orcid.org/0000-0001-6157-214X; Email: samantha.husmann@leibniz-inm.de

Author

Behnoosh Bornamehr − *INM—Leibniz Institute for New Materials, 66123 Saarbrücken, Germany; Department of Materials Science & Engineering, Saarland University, 66123 Saarbrücken, Germany*

Complete contact information is available at: https://pubs.acs.org/10.1021/acsomega.2c04209

Author Contributions

B.B.: methodology, investigation, data curation, validation, writing—original draft. V.P.: methodology, validation, supervision, funding acquisition, visualization, writing—review and editing. S.H.: conceptualization, methodology, validation, supervision, funding acquisition, writing—review and editing.

Notes

The authors declare no competing financial interest.

■ ACKNOWLEDGMENTS

S.H. acknowledges funding of the PBDS project (HU 2959/2) by the German Research Foundation (DFG, Deutsche Forschungsgemeinschaft). The authors thank Eduard Arzt (INM) for his continuing support.

■ REFERENCES

(1) Moeller, K.-C.Overview of Battery Systems. In *Lithium-Ion Batteries: Basics and Applications*; Korthauer, R., Ed.; Springer, 2018; pp 5−9.

(2) Leuthner, S.Lithium-Ion Battery Overview. In *Lithium-Ion Batteries: Basics and Applications*; Korthauer, R., Ed.; Springer, 2018; pp 14−17.

(3) Guney, M. S.; Tepe, Y. Classification and assessment of energy storage systems. *Renewable Sustainable Energy Rev.* **2017**, *75*, 1187−1197.
(4) Zhou, H.; Xin, F.; Pei, B.; Whittingham, M. S. What limits the capacity of layered oxide cathodes in lithium batteries? *ACS Energy Lett.* **2019**, *4*, 1902−1906.
(5) Manthiram, A.; Song, B.; Li, W. A perspective on nickel-rich layered oxide cathodes for lithium-ion batteries. *Energy Storage Mater.* **2017**, *6*, 125−139.
(6) Xie, D.; Mei, S.; Xu, Y.; Quan, T.; Härk, E.; Kochovski, Z.; Lu, Y. Efficient sulfur host based on yolk-shell iron oxide/sulfide-carbon nanospindles for lithium-sulfur batteries. *ChemSusChem* **2021**, *14*, 1404−1413.
(7) Hu, Z.; Liu, Q.; Chou, S.-L.; Dou, S.-X. Advances and challenges in metal sulfides/selenides for next-generation rechargeable sodium-ion batteries. *Adv. Mater.* **2017**, *29*, No. 1700606.
(8) Yu, X. Y.; Lou, X. W. Mixed metal sulfides for electrochemical energy storage and conversion. *Adv. Energy Mater.* **2018**, *8*, No. 1701592.
(9) Goodenough, J. B. Energy storage materials: a perspective. *Energy Storage Mater.* **2015**, *1*, 158−161.
(10) Nitta, N.; Wu, F.; Lee, J. T.; Yushin, G. Li-ion battery materials: present and future. *Mater. Today* **2015**, *18*, 252−264.
(11) Huang, X.; Tang, J.; Luo, B.; Knibbe, R.; Lin, T.; Hu, H.; Rana, M.; Hu, Y.; Zhu, X.; Gu, Q.; et al. Sandwich-like ultrathin TiS_2 nanosheets confined within N, S codoped porous carbon as an effective polysulfide promoter in lithium-sulfur batteries. *Adv. Energy Mater.* **2019**, *9*, No. 1901872.
(12) Liu, Y.; Che, Z.; Lu, X.; Zhou, X.; Han, M.; Bao, J.; Dai, Z. Nanostructured metal chalcogenides confined in hollow structures for promoting energy storage. *Nanoscale Adv.* **2020**, *2*, 583−604.
(13) Ding, W.; Wang, X.; Peng, H.; Hu, L. Electrochemical performance of the chalcopyrite $CuFeS_2$ as cathode for lithium ion battery. *Mater. Chem. Phys.* **2013**, *137*, 872−876.
(14) Theerthagiri, J.; Senthil, R. A.; Nithyadharseni, P.; Lee, S. J.; Durai, G.; Kuppusami, P.; Madhavan, J.; Choi, M. Y. Recent progress and emerging challenges of transition metal sulfides based composite electrodes for electrochemical supercapacitive energy storage. *Ceram. Int.* **2020**, *46*, 14317−14345.
(15) Wang, Y.; Li, X.; Zhang, Y.; He, X.; Zhao, J. Ether based electrolyte improves the performance of $CuFeS_2$ spike-like nanorods as a novel anode for lithium storage. *Electrochim. Acta* **2015**, *158*, 368−373.
(16) Wang, Q.; Jin, J.; Wu, X.; Ma, G.; Yang, J.; Wen, Z. A shuttle effect free lithium sulfur battery based on a hybrid electrolyte. *Phys. Chem. Chem. Phys.* **2014**, *16*, 21225−21229.
(17) Ge, P.; Zhang, L.; Zhao, W.; Yang, Y.; Sun, W.; Ji, X. Interfacial bonding of metal-sulfides with double carbon for improving reversibility of advanced alkali-ion batteries. *Adv. Funct. Mater.* **2020**, *30*, No. 1910599.
(18) Budak, Ö.; Srimuk, P.; Aslan, M.; Shim, H.; Borchardt, L.; Presser, V. Titanium niobium oxide $Ti_2Nb_{10}O_{29}$/carbon hybrid electrodes derived by mechanochemically synthesized carbide for high-performance lithium-ion batteries. *ChemSusChem* **2021**, *14*, 398−407.
(19) Shim, H.; Lim, E.; Fleischmann, S.; Quade, A.; Tolosa, A.; Presser, V. Nanosized titanium niobium oxide/carbon electrodes for lithium-ion energy storage applications. *Sustainable Energy Fuels* **2019**, *3*, 1776−1789.
(20) Zhao, Y.; Wang, L. P.; Sougrati, M. T.; Feng, Z.; Leconte, Y.; Fisher, A.; Srinivasan, M.; Xu, Z. A review on design strategies for carbon based metal oxides and sulfides nanocomposites for high performance Li and Na ion battery anodes. *Adv. Energy Mater.* **2017**, *7*, No. 1601424.
(21) Husmann, S.; Zarbin, A. J. G.; Dryfe, R. A. W. High-performance aqueous rechargeable potassium batteries prepared via interfacial synthesis of a Prussian blue-carbon nanotube composite. *Electrochim. Acta* **2020**, *349*, No. 136243.
(22) Zakaria, M. B.; Chikyow, T. Recent advances in Prussian blue and Prussian blue analogues: synthesis and thermal treatments. *Coord. Chem. Rev.* **2017**, *352*, 328−345.
(23) Guo, Y.; Tang, J.; Wang, Z.; Sugahara, Y.; Yamauchi, Y. Hollow porous heterometallic phosphide nanocubes for enhanced electrochemical water splitting. *Small* **2018**, *14*, No. 1802442.
(24) Nai, J.; Lou, X. W. Hollow structures based on Prussian blue and its analogs for electrochemical energy storage and conversion. *Adv. Mater.* **2019**, *31*, No. 1706825.
(25) Kang, B. K.; Woo, M. H.; Lee, J.; Song, Y. H.; Wang, Z.; Guo, Y.; Yamauchi, Y.; Kim, J. H.; Lim, B.; Yoon, D. H. Mesoporous Ni−Fe oxide multi-composite hollow nanocages for efficient electrocatalytic water oxidation reactions. *J. Mater. Chem. A* **2017**, *5*, 4320−4324.
(26) Wu, X.; Ru, Y.; Bai, Y.; Zhang, G.; Shi, Y.; Pang, H. PBA composites and their derivatives in energy and environmental applications. *Coord. Chem. Rev.* **2022**, *451*, No. 214260.
(27) Zhong, L.; Mao, B.; Liu, M.; Liu, M.; Sun, Y.; Song, Y.-T.; Zhang, Z.-M.; Lu, T.-B. Construction of hierarchical photocatalysts by growing $ZnIn_2S_4$ nanosheets on Prussian blue analogue-derived bimetallic sulfides for solar co-production of H_2 and organic chemicals. *J. Energy Chem.* **2021**, *54*, 386−394.
(28) Song, X.; Song, S.; Wang, D.; Zhang, H. Prussian blue analogs and their derived nanomaterials for electrochemical energy storage and electrocatalysis. *Small Methods* **2021**, *5*, No. 2001000.
(29) Chen, X.; Zeng, S.; Muheiyati, H.; Zhai, Y.; Li, C.; Ding, X.; Wang, L.; Wang, D.; Xu, L.; He, Y.; Qian, Y. Double-shelled Ni−Fe−P/N-doped carbon nanobox derived from a prussian blue analogue as an electrode material for K-ion batteries and Li−S batteries. *ACS Energy Lett.* **2019**, *4*, 1496−1504.
(30) Peng, Z.; Qiu, X. Y.; Yu, Y.; Jiang, D.; Wang, H. T.; Cai, G. Y.; Zhang, X. X.; Dong, Z. H. Polydopamine coated Prussian blue analogue derived hollow carbon nanoboxes with FeP encapsulated for hydrogen evolution. *Carbon* **2019**, *152*, 16−23.
(31) Ming, H.; Torad, N. L.; Chiang, Y.-D.; Wu, K. C.-W.; Yamauchi, Y. Size-and shape-controlled synthesis of Prussian Blue nanoparticles by a polyvinylpyrrolidone-assisted crystallization process. *CrystEngComm* **2012**, *14*, 3387−3396.
(32) Lopes, L. C.; Husmann, S.; Zarbin, A. J. G. Chemically synthesized graphene as a precursor to Prussian blue-based nanocomposite: A multifunctional material for transparent aqueous K-ion battery or electrochromic device. *Electrochim. Acta* **2020**, *345*, No. 136199.
(33) Husmann, S.; Booth, S. G.; Zarbin, A. J. G.; Dryfe, R. A. W. Electrodeposition of Prussian blue/carbon nanotube composites at a liquid-liquid interface. *J. Braz. Chem. Soc.* **2018**, *29*, 1130−1139.
(34) Li, W.-J.; Han, C.; Cheng, G.; Chou, S.-L.; Liu, H.-K.; Dou, S.-X. Chemical properties, structural properties, and energy storage applications of prussian blue analogues. *Small* **2019**, *15*, No. 1900470.
(35) Husmann, S.; Orth, E. S.; Zarbin, A. J. G. A multi-technique approach towards the mechanistic investigation of the electrodeposition of Prussian blue over carbon nanotubes film. *Electrochim. Acta* **2019**, *312*, 380−391.
(36) Hurlbutt, K.; Wheeler, S.; Capone, I.; Pasta, M. Prussian blue analogs as battery materials. *Joule* **2018**, *2*, 1950−1960.
(37) Liu, Y.; Ai, K.; Lu, L. Polydopamine and its derivative materials: synthesis and promising applications in energy, environmental, and biomedical fields. *Chem. Rev.* **2014**, *114*, 5057−5115.
(38) Ryu, J. H.; Messersmith, P. B.; Lee, H. Polydopamine surface chemistry: A decade of discovery. *ACS Appl. Mater. Interfaces* **2018**, *10*, 7523−7540.
(39) Liebscher, J.; Mrówczyński, R.; Scheidt, H. A.; Filip, C.; Hădade, N. D.; Turcu, R.; Bende, A.; Beck, S. Structure of polydopamine: a never-ending story? *Langmuir* **2013**, *29*, 10539−10548.
(40) Yang, J.; Stuart, M. A. C.; Kamperman, M. Jack of all trades: versatile catechol crosslinking mechanisms. *Chem. Soc. Rev.* **2014**, *43*, 8271−8298.

https://doi.org/10.1021/acsomega.2c04209
ACS Omega 2022, 7, 38674−38685

(41) Zeng, H.; Hwang, D. S.; Israelachvili, J. N.; Waite, J. H. Strong reversible Fe^{3+}-mediated bridging between dopa-containing protein films in water. *Proc. Natl. Acad. Sci. U.S.A.* **2010**, *107*, 12850−12853.
(42) Holten-Andersen, N.; Harrington, M. J.; Birkedal, H.; Lee, B. P.; Messersmith, P. B.; Lee, K. Y. C.; Waite, J. H. pH-induced metal-ligand cross-links inspired by mussel yield self-healing polymer networks with near-covalent elastic moduli. *Proc. Natl. Acad. Sci. U.S.A.* **2011**, *108*, 2651−2655.
(43) Moretti, G.; Gervais, C. Raman spectroscopy of the photosensitive pigment Prussian blue. *J. Raman Spectrosc.* **2018**, *49*, 1198−1204.
(44) Kettle, S. F. A.; Diana, E.; Marchese, E. M. C.; Boccaleri, E.; Stanghellini, P. L. The vibrational spectra of the cyanide ligand revisited: the ν(CN) infrared and Raman spectroscopy of Prussian blue and its analogues. *J. Raman Spectrosc.* **2011**, *42*, 2006−2014.
(45) Ojwang, D. O.; Grins, J.; Wardecki, D.; Valvo, M.; Renman, V.; Häggström, L.; Ericsson, T.; Gustafsson, T.; Mahmoud, A.; Hermann, R. P.; Svensson, G. Structure characterization and properties of K-containing copper hexacyanoferrate. *Inorg. Chem.* **2016**, *55*, 5924−5934.
(46) Figueiredo, M. L.; Martin, C. S.; Furini, L. N.; Rubira, R. J.; Batagin-Neto, A.; Alessio, P.; Constantino, C. J. Surface-enhanced Raman scattering for dopamine in Ag colloid: Adsorption mechanism and detection in the presence of interfering species. *Appl. Surf. Sci.* **2020**, *522*, No. 146466.
(47) Asakura, D.; Okubo, M.; Mizuno, Y.; Kudo, T.; Zhou, H.; Ikedo, K.; Mizokawa, T.; Okazawa, A.; Kojima, N. Fabrication of a cyanide-bridged coordination polymer electrode for enhanced electrochemical ion storage ability. *J. Phys. Chem. C* **2012**, *116*, 8364−8369.
(48) Wu, X.; Luo, Y.; Sun, M.; Qian, J.; Cao, Y.; Ai, X.; Yang, H. Low-defect Prussian blue nanocubes as high capacity and long life cathodes for aqueous Na-ion batteries. *Nano Energy* **2015**, *13*, 117−123.
(49) Yu, X.; Fan, H.; Liu, Y.; Shi, Z.; Jin, Z. Characterization of carbonized polydopamine nanoparticles suggests ordered supramolecular structure of polydopamine. *Langmuir* **2014**, *30*, 5497−5505.
(50) Parker, G. K.; Woods, R.; Hope, G. A. Raman investigation of chalcopyrite oxidation. *Colloids Surf., A* **2008**, *318*, 160−168.
(51) Ohrendorf, F.; Haeuseler, H. Lattice dynamics of chalcopyrite type compounds. Part I. Vibrational frequencies. *Cryst. Res. Technol.* **1999**, *34*, 339−349.
(52) Mernagh, T. P.; Trudu, A. G. A laser Raman microprobe study of some geologically important sulphide minerals. *Chem. Geol.* **1993**, *103*, 113−127.
(53) Jiang, F.; Zhao, W.; Zhang, L.; Tian, Y.; Gao, X.; Ge, P.; Sun, W.; Chang, X.; Ji, X. Unraveling the mechanism of chalcopyrite's superior performance for lithium storage. *ACS Appl. Energy Mater.* **2021**, *4*, 5086−5093.
(54) Conejeros, S.; Alemany, P.; Llunell, M.; Sanchez, V.; Llanos, J.; Padilla-Campos, L. Structural stability of quaternary $ACuFeS_2$ (A= Li, K) phases: a computational approach. *Inorg. Chem.* **2012**, *51*, 362−369.
(55) Wu, X.; Zhao, Y.; Yang, C.; He, G. PVP-assisted synthesis of shape-controlled $CuFeS_2$ nanocrystals for Li-ion batteries. *J. Mater. Sci.* **2015**, *50*, 4250−4257.
(56) Guo, P.; Song, H.; Liu, Y.; Wang, C. $CuFeS_2$ quantum dots anchored in carbon frame: superior lithium storage performance and the study of electrochemical mechanism. *ACS Appl. Mater. Interfaces* **2017**, *9*, 31752−31762.
(57) Sun, W.; Tao, X.; Du, P.; Wang, Y. Carbon-coated mixed-metal sulfide hierarchical structure: MOF-derived synthesis and lithium-storage performances. *Chem. Eng. J.* **2019**, *366*, 622−630.
(58) Husmann, S.; Budak, Ö.; Quade, A.; Frank, A.; Kruth, A.; Scheu, C.; Tolosa, A.; Presser, V. Electrospun vanadium sulfide / carbon hybrid fibers obtained via one-step thermal sulfidation for use as lithium-ion battery electrodes. *J. Power Sources* **2020**, *450*, No. 227674.
(59) Cho, Y.-D.; Fey, G. T.-K.; Kao, H.-M. The effect of carbon coating thickness on the capacity of LiFePO4/C composite cathodes. *J. Power Sources* **2009**, *189*, 256−262.
(60) Smith, A. J.; Burns, J.; Dahn, J. A high precision study of the Coulombic efficiency of Li-ion batteries. *Electrochem. Solid-State Lett.* **2010**, *13*, A177.
(61) Zhu, Z.; Cheng, F.; Chen, J. Investigation of effects of carbon coating on the electrochemical performance of Li 4 Ti 5 O 12/C nanocomposites. *J. Mater. Chem. A* **2013**, *1*, 9484−9490.
(62) Li, R.; Wang, Y.; Zhou, C.; Wang, C.; Ba, X.; Li, Y.; Huang, X.; Liu, J. Carbon-stabilized high-capacity ferroferric oxide nanorod array for flexible solid-state alkaline battery−supercapacitor hybrid device with high environmental suitability. *Adv. Funct. Mater.* **2015**, *25*, 5384−5394.
(63) Zhang, Y.; Zhao, G.; Lv, X.; Tian, Y.; Yang, L.; Zou, G.; Hou, H.; Zhao, H.; Ji, X. Exploration and size engineering from natural chalcopyrite to high-performance electrode materials for lithium-ion batteries. *ACS Appl. Mater. Interfaces* **2019**, *11*, 6154−6165.
(64) Wu, M.; Zhang, Y.; Li, T.; Chen, Z.; Cao, S.-a.; Xu, F. Copper sulfide nanoparticles as high-performance cathode materials for magnesium secondary batteries. *Nanoscale* **2018**, *10*, 12526−12534.
(65) Zheng, S.; Yi, F.; Li, Z.; Zhu, Y.; Xu, Y.; Luo, C.; Yang, J.; Wang, C. Copper-stabilized sulfur-microporous carbon cathodes for Li−S batteries. *Adv. Funct. Mater.* **2014**, *24*, 4156−4163.
(66) McDowell, M. T.; Lu, Z.; Koski, K. J.; Yu, J. H.; Zheng, G.; Cui, Y. In situ observation of divergent phase transformations in individual sulfide nanocrystals. *Nano Lett.* **2015**, *15*, 1264−1271.
(67) Shi, C.; Li, X.; He, X.; Zhao, J. New insight into the interaction between carbonate-based electrolyte and cuprous sulfide electrode material for lithium ion batteries. *Electrochim. Acta* **2015**, *174*, 1079−1087.
(68) Lu, J.; Lian, F.; Guan, L.; Zhang, Y.; Ding, F. Adapting FeS_2 micron particles as an electrode material for lithium-ion batteries via simultaneous construction of CNT internal networks and external cages. *J. Mater. Chem. A* **2019**, *7*, 991−997.

https://doi.org/10.1021/acsomega.2c04209
ACS Omega 2022, 7, 38674−38685